Experimental quantum position verification: practical challenges and single-photon correlations

Kanneworff, K.N.

4 Hong-Ou-Mandel interference in a realistic unbalanced Mach-Zehnder interferometer

To characterize the indistinguishability of quantum-dot-based and other single-photon sources, often, sequential photons are interfered in an unbalanced Mach-Zehnder interferometer, where Hong-Ou-Mandel two-photon quantum interference is used to determine the single-photon indistinguishability. However, these photon correlations contain more information than just the single-photon indistinguishability, in particular if two-photon correlation events occur with time delay $\Delta\tau$ equal to the internal delay t_d of the interferometer. We give here a didactic description and derivation of those correlations at $\Delta\tau = \pm t_d$, and derive an expression of the photon indistinguishability for the generic case of imperfect beam splitters and other experimental imperfections. We validate our theory by comparison to literature and to experimental measurements with photons produced by a InGaAs/GaAs quantum dot – microcavity single-photon source.

4.1 Introduction

High single-photon indistinguishability is an important requirement for most applications quantum optics that rely on two-photon Hong-Ou-Mandel (HOM) interference, including linear optical quantum computing and quantum networks [57–59]. To characterize the photon indistinguishability of a source, it is common to use an unbalanced Mach-Zehnder interferometer (MZI) [60–65], in which consecutive single photons are probabilistically split by the first beam splitter, synchronized with later photons via a time delay, and then made to interfere at the second beam splitter. Depending on their mutual indistinguishability, or equivalently the overlap of their wave functions across all degrees of freedom, HOM interference leading to photon bunching may or may not occur. This effect can be readily observed using two single-photon detectors at the output of the second beam splitter.

The measured photon correlations at zero time delay provide a measure of the degree of indistinguishability of the single-photon source. These measurements can also be done for delays much larger than the time between consecutively produced single-photons in order to probe decoherence of the single-photon source on longer time-scales [66, 67].

For both short and long delays, the measured two-photon correlations exhibit features not only at zero time delay but also at a delay equal to the path length difference of the interferometer [66, 68]. These additional features have recently been shown to contain information about the photon-number coherence of the source [69, 70], but they also appear for perfect single-photon sources without photon-number coherence. In the first part of this chapter, we give an intuitive qualitative explanation of these features and correlations. Moreover, most existing analyses assume an idealized, perfectly symmetric (balanced in intensity) MZI, which is often not the case.

To address these challenges, we first dive deeper into the cause of the additional features in the correlation measurements. We then develop a comprehensive analytical framework that describes two-photon interference in an MZI as a function of all relevant experimental parameters, including intensity imbalance in the interferometer and experimental errors in the wavefunction overlap which is tuned by the polarization state of the photons. We validate our analytical framework by comparison to literature and to two-photon correlation measurements performed with our quantum dot – microcavity single-photon source [71, 72].

4.2 Theory

A two-photon correlation measurement using an MZI is presented in Fig. 4.1, where the measured coincidence counts are shown as a function of the time delay $\Delta\tau$ between detection events. The three different colors represent three different regimes of correlations: red are the correlations corresponding to the two detectors clicking simultaneously ($\Delta\tau = 0$), purple corresponds to $\Delta\tau = \pm t_d$ the delay in the MZI which is here equal to the temporal separation of the single-photon wavepackets τ_l, and blue are other correlations. We clearly observe that the purple coincidence peaks are lower than the blue ones, and the red peak is even lower. This latter is a signature of HOM photon bunching, where two photons predominantly exit the final beam splitter "bunched" together and result in reduced coincidences.

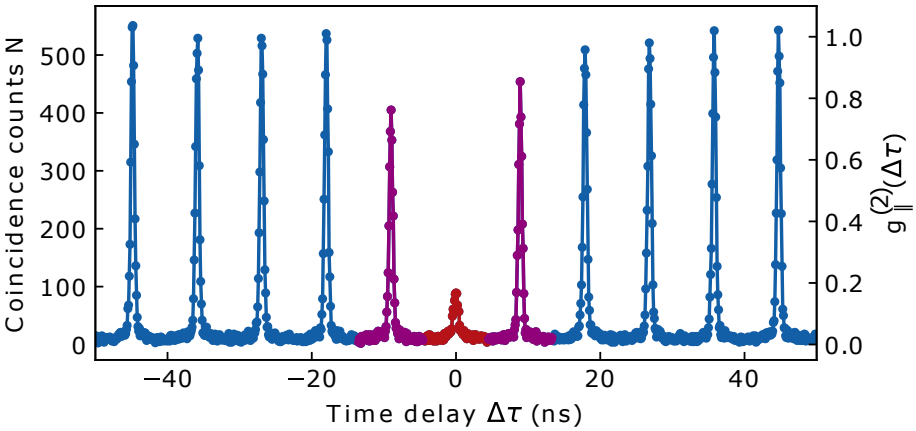

Figure 4.1: Example of a two-photon correlation measurement as a function of the time delay between detection events to determine the indistinguishability of a quantum dot single-photon source. The left axis shows the raw coincidence counts and on the right axis we show the normalized $g^{(2)}$. For this particular example, the delay in the Mach-Zehnder interferometer is equal to the pulse period of $\tau_l = 9$ ns. The three different colors represent three different regimes of correlations: red are the correlations corresponding to the two detectors clicking simultaneously ($\Delta\tau = 0$), purple corresponds to $\Delta\tau = \pm t_d$ the delay in the MZI, and blue are all other correlations.

4.2.1 The ideal Mach-Zehnder interferometer

First we explain in detail why the correlations at $\Delta\tau = \pm t_d$ are lower than all other $\Delta\tau \neq 0$ correlations. To simplify the explanation we assume that the MZI is ideal, i.e. has perfectly balanced splitting ratios and equal transmission in both interferometer arms. Furthermore, we set the delay between the short and long arm of the interferometer t_d to be equal to the time between two consecutive photons in the single-photon stream τ_l, as is the case for the measurement shown in Fig. 4.1. A schematic of this simplified MZI is shown in Fig. 4.2(a) consisting of two beam splitters (BS_1, BS_2) and two single-photon detectors (D1, D2). The numbers (1), (2) and (3) denote different locations in the interferometer for which we show a cartoon of the single-photon stream in Fig. 4.2(b). (1) is before the first beam splitter BS_1, (2) is just after splitting the single-photon stream and (3) is after temporal synchronization before the photons interfere at BS_2.

Before entering the interferometer (1) there is a stream of single-photons (●) separated by τ_l. In this example we only describe the photon statistics with respect to the photon depicted by blue dot ● in the stream. After the 50:50 beam splitter (2) the photons are in superposition between the two arms of the interferometer (○) and after the delay (3), the photons in the long arm of the interferometer are delayed by t_d, which in this case is equal to the temporal separation of the photons τ_l. Now we have to distinguish two cases of photon trajectories: one where the photon ● went through the short arm of the interferometer and another where it went through the long arm. If the photon went into the short arm, there has to be an empty time bin at $+t_d$ in the long arm, because this is where the photon would have been if it had taken the longer path. Similarly, if the photon went into the the long path there has to be an empty time bin at $-t_d$ in the short arm. Consequently, there is always one trajectory less that leads to a coincidence detection at $\pm t_d$ time delay compared to all other non-zero delays. Because there are generally four

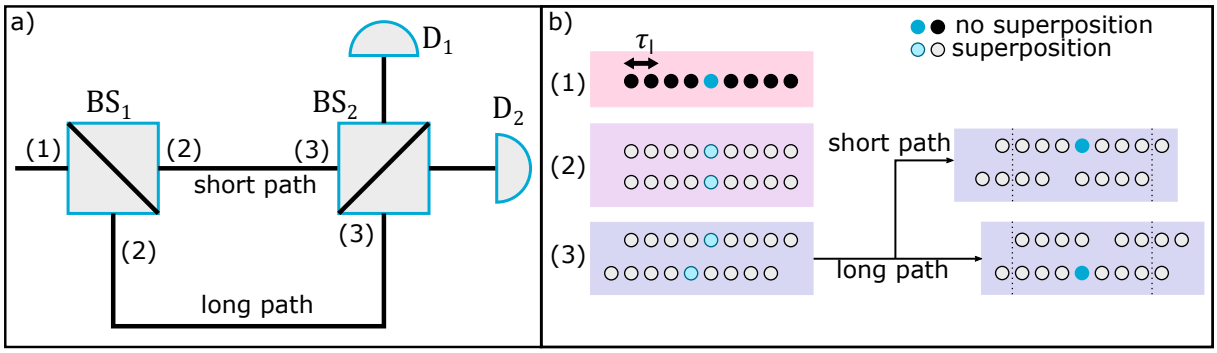

Figure 4.2: Ideal Mach-Zehnder interferometer and photon correlations. (a) schematic of the MZI, (b) cartoon of the photon streams before the first beam splitter (1), just after the first beam splitter (2) and after the temporal delay in the lower arm (3), where the delay τ_d between the arms is equal to the time between consecutive photons τ_l. A blue color indicates an arbitrarily chosen photon, and upper/lower streams indicate upper/lower paths. Empty circles indicate photons in superposition between different paths.

possible photon trajectories that lead to coincidence detection at non-zero time delay, the peaks corresponding to $\pm t_d$ have a height of 3/4 instead of 1.

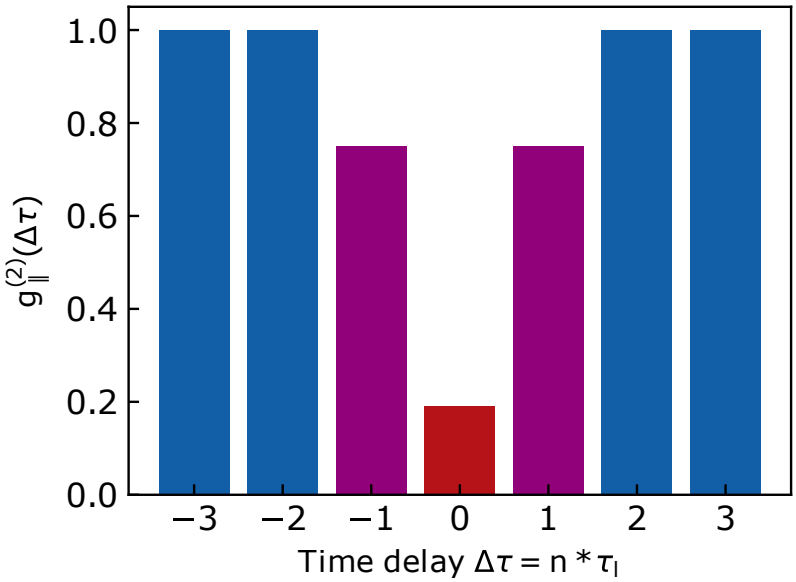

Figure 4.3: Theoretical correlations in the simplified MZI where the red bar corresponds to zero time-delay correlations indicating imperfect indistinguishability as present in the experimental data in Fig. 4.1, the purple bars corresponds to correlations at time differences equal to the time delay of the MZI arms, and all other correlations are shown in blue. The detection time delay $\Delta\tau$ is shown as integer multiples of the period between two consecutive photons in the initial single-photon stream, $n \cdot \tau_l$.

We visualize this result in Fig. 4.3, where the normalized $g^{(2)}(\Delta\tau)$ is shown for this particular example. The red bar at $\Delta\tau = 0$ is set to match with the experimental value shown in Fig. 4.1 and is absent for perfectly indistinguishable photons. However, we

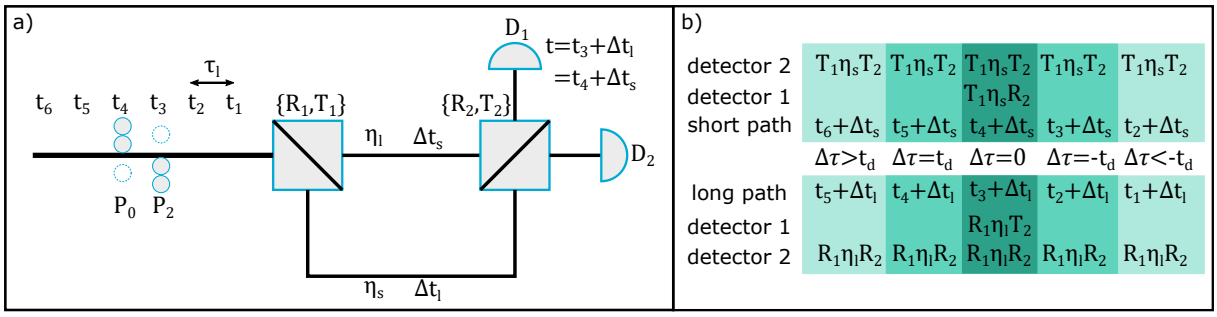

Figure 4.4: A realistic Mach-Zehnder interferometer. (a) Schematic representation of the interferometer with imperfect beam splitters with reflectivity R and transmission T, and finite transmission through the interferometer arms η. (b) shows time bins and possible photon trajectories, including which experimental parameters the photons experience.

note that the explanation of correlations at $\Delta\tau = \pm t_d$ (purple) is independent on the photon indistinguishability or wavefunction overlap of the photons since the detection events do not occur simultaneously and hence no interference effects take place (if there is not photon-number coherence).

We see that the purple side-peaks at $\Delta\tau = \pm t_d$ of our experimental results in Fig. 4.1 deviate from the theoretical prediction in Fig. 4.3, the height of the peaks surpass 0.75 and are not equal. Furthermore, we observe that the peaks for $|\Delta\tau| > t_d$ are not exactly equal to one and fluctuate. The latter can be explained by shot noise caused by non-ideal photon generation and detection. The former is caused by imperfections in the Mach-Zehnder interferometer as we will show now.

4.2.2 A realistic Mach-Zehnder interferometer

Parameters and assumptions

A schematic representation of a realistic Mach-Zehnder interferometer is shown in Fig. 4.4. At the input of the interferometer, we consider a photon stream with six time bins $t_1 ... t_6$. For each time bin, we describe the photonic state by an incoherent mixture of zero, one, and two photons using the density matrix $\rho = P_0|0\rangle\langle 0| + P_1|1\rangle\langle 1| + P_2|2\rangle\langle 2|$, where P_0, P_1 and P_2 are the probabilities of 0, 1 or 2 photons. We assume that these probabilities do not change with time and that the single-photon source exhibits low brightness such that: $P_0 \gg P_1 \gg P_2$ with $P_0 \approx 1$. The first beam splitter of the interferometer (BS_1) distributes the photon stream over the arms of the MZI, in the shorter arm they experience a temporal delay of Δt_s with a transmission of η_s, and in the longer arm a delay of Δt_l with transmission η_l. The temporal delay between the two arms t_d is set, in this example, to the time difference between two consecutive photons τ_l, i.e., $t_d = \tau_l = \Delta t_l - \Delta t_s = t_4 - t_3$. The second beam splitter (BS_2) recombines the two arms of the interferometer, and detectors D1 and D2 are used for coincidence detection.

Without restricting generality, we now only take correlations into account with respect to a detection event of D1 at time t where $t = t_3 + \Delta t_l = t_4 + \Delta t_s$, meaning that it was caused either by a photon created at time t_3 which had taken the long arm of the interferometer (probability $P_1 R_1 \eta_l$) or a photon that was created at t_4 that had taken the short path (probability $P_1 T_1 \eta_s$). In order to result in a detection event by detector

D1, a photon from the short path should be reflected by BS_2 (R_2) or transmitted (T_2) if the photon came from the long path. To describe these photon trajectories we use the following notation:

$$\begin{aligned}(t_3 + \Delta t_l)_{D1} &: P_1 R_1 \eta_l T_2 \\ (t_4 + \Delta t_s)_{D1} &: P_1 T_1 \eta_s R_2\end{aligned} \tag{4.1}$$

These photon trajectories are also depicted in Fig. 4.4(b).

We now calculate the correlations as a function of the detection time difference $\Delta\tau$ and now consider three different cases: In the first case, both detectors click simultaneously ($\Delta\tau = 0$), the second one is where the delay between click events is equal to the delay between the arms of the MZI ($\Delta\tau = \pm t_d$) and the last case are the correlations for all other $\Delta\tau$. In the particular example given in Fig. 4.4 we consider the last case to be $\Delta\tau = \pm 2t_d$; this choice has no influence on the outcome of the discussion.

Uncorrelated coincidences at $\Delta\tau = \pm 2t_d$

These coincidences are used for normalization of the second-order correlation function. For now we focus only on the case where detector D2 clicks after D1. As shown in Fig. 4.4(b), there are two options that lead to a click at detector D2 at a time difference of $\Delta\tau = 2t_d$, namely a photon created at t_5 taking the long arm and a photon created at time t_6 taking the short arm. However, the operation by the second beam splitter is now mirrored, since states moving through the short arm now need to be transmitted by the second beam splitter to arrive at D2 and reflected if they traveled through the longer arm. These two possible options for D2 in combination with the two options for a click at time t by D1 results in four contributing terms:

$$\begin{aligned}(t_3 + \Delta t_l)_{D1}\,(t_5 + \Delta t_l)_{D2} &: P_1^2 R_1^2 \eta_l^2 T_2 R_2 \\ (t_3 + \Delta t_l)_{D1}\,(t_6 + \Delta t_s)_{D2} &: P_1^2 R_1 \eta_l T_1 \eta_s R_2^2 \\ (t_4 + \Delta t_s)_{D1}\,(t_5 + \Delta t_l)_{D2} &: P_1^2 T_1 \eta_s R_1 \eta_l T_2^2 \\ (t_4 + \Delta t_s)_{D1}\,(t_6 + \Delta t_s)_{D2} &: P_1^2 T_1^2 \eta_s^2 T_2 R_2\end{aligned} \tag{4.2}$$

The total uncorrelated coincidences probability $A_\pm$ is the sum of the four contributions:

$$A_\pm = P_1^2 \left\{ R_2 T_2 \left(R_1^2 \eta_l^2 + T_1^2 \eta_s^2 \right) + T_1 \eta_s R_1 \eta_l \left(T_2^2 + R_2^2 \right) \right\} \tag{4.3}$$

The case where $\Delta\tau = -2t_d$, detector D2 clicks before D1 does, follows the same reasoning and results in the exact same expression.

Reduced coincidences at $\Delta\tau = \pm t_d$

In order to calculate the correlations at $\Delta\tau = t_d = \Delta t_l - \Delta t_s$, we again first only consider a positive delay where D1 clicks before D2 does, which again consists of four contributions:

$$\begin{aligned}(t_3 + \Delta t_l)_{D1}\,(t_4 + \Delta t_l)_{D2} &: P_1^2 R_1^2 \eta_l^2 R_2 T_2 \\ (t_4 + \Delta t_s)_{D1}\,(t_5 + \Delta t_s)_{D2} &: P_1^2 T_1^2 \eta_s^2 R_2 T_2 \\ (t_3 + \Delta t_l)_{D1}\,(t_5 + \Delta t_s)_{D2} &: P_1^2 R_1 \eta_l T_1 \eta_s T_2^2 \\ (t_4 + \Delta t_s)_{D1}\,(t_4 + \Delta t_l)_{D2} &: P_1^2 g^{(2)}(0) R_1 \eta_l T_1 \eta_s R_2^2\end{aligned} \tag{4.4}$$

The first three terms of Equation 4.4 are similar in nature to the four contributions for the previous regime where $\Delta\tau = \pm 2t_d$ (Eq. 4.2). However, the last term can only occur if two photons are created at time t_4 and that move through opposite arms of the interferometer. Under the assumption that a maximum of two photons are distributed over the six possible time bins, we can describe this multi-photon component in two time bins by P_0P_2. Under the assumptions the photon statistics of the source does not change over time, and a low brightness in combination with the expression for the Hanbury Brown and Twiss (HBT) second-order correlation function $g^{(2)}(0) = \frac{2P_2}{(P_1+2P_2)^2}$ we can state that $P_2P_0 \approx \frac{1}{2}g^{(2)}(0)P_1^2$. Furthermore, since it does not matter which of the two photons enters which path, as long as they take opposite arms of the interferometer, we gain an additional factor 2 resulting in the expression seen in the last term of Equation 4.4.

This means that for $\Delta\tau = t_d$ we obtain for the total coincidence probability

$$A_{t_d} = P_1^2 \left\{ R_2T_2 \left(R_1^2\eta_l^2 + T_1^2\eta_s^2 \right) + R_1\eta_l T_1\eta_s \left(T_2^2 + g^{(2)}(0)R_2^2 \right) \right\}. \tag{4.5}$$

Similarly, we can derive the expression for coincidences at $\Delta\tau = -t_d$ where D2 clicks before D1 and obtain

$$A_{-t_d} = P_1^2 \left\{ R_2T_2 \left(R_1^2\eta_l^2 + T_1^2\eta_s^2 \right) + T_1\eta_s R_1\eta_l \left(g^{(2)}(0)T_2^2 + R_2^2 \right) \right\}. \tag{4.6}$$

The reason why the multi-photon contribution has moved to the T_2^2 term is that this contribution belongs to the term $(t_3 + \Delta t_l)_{D1}(t_3 + \Delta t_s)_{D2}$ which requires both photons to be transmitted by the second beam splitter.

Coincidences at $\Delta\tau = 0$

Finally, we discuss the case that detectors D1 and D2 are clicking simultaneously. Following an analogous procedure as before we obtain 4 contributions:

$$\begin{aligned} &(t_3 + \Delta t_l)_{D1}(t_3 + \Delta t_l)_{D2} \\ &(t_4 + \Delta t_s)_{D1}(t_4 + \Delta t_s)_{D2} \\ &(t_3 + \Delta t_l)_{D1}(t_4 + \Delta t_s)_{D2} \\ &(t_4 + \Delta t_s)_{D1}(t_3 + \Delta t_l)_{D2} \end{aligned} \tag{4.7}$$

The first two contributions stem from two photons created in the same time bin which traveled through the same arm of the interferometer, arriving at different detectors. Hence, they can be written in a similar way to the multi-photon component derived for the case $\Delta\tau = \pm t_d$:

$$\begin{aligned} &(t_3 + \Delta t_l)_{D1}(t_3 + \Delta t_l)_{D2} : g^{(2)}(0)P_1^2R_1^2\eta_l^2R_2T_2 \\ &(t_4 + \Delta t_s)_{D1}(t_4 + \Delta t_s)_{D2} : g^{(2)}(0)P_1^2T_1^2\eta_s^2R_2T_2 \end{aligned} \tag{4.8}$$

The last two terms in Eq. 4.7 imply that one photon was created at time t_3 and the other at time t_4. Naively one would use the same method as for $\Delta\tau = \pm 2t_d$:

$$\begin{aligned} &(t_3 + \Delta t_l)_{D1}(t_4 + \Delta t_s)_{D2} : P_1^2R_1\eta_l T_1\eta_s T_2^2 \\ &(t_4 + \Delta t_s)_{D1}(t_3 + \Delta t_l)_{D2} : P_1^2R_1\eta_l T_1\eta_s R_2^2 \end{aligned} \tag{4.9}$$

However, these expressions are only valid under the assumptions that the two photons are fully distinguishable and no HOM quantum interference takes place at the second

beam splitter. If the photons are fully indistinguishable, the probability of both detectors clicking simultaneously is dependent only on the asymmetry in splitting ratio of the last beam splitter (BS_2). The expression for the correlations at $\Delta\tau = 0$ is again the sum of the four contributions, but contrary to the previous two regimes ($\Delta\tau = \pm 2t_d$, $\Delta\tau = \pm t_d$) here we differentiate between photons being either fully indistinguishable ($A_{0\parallel}$) or fully distinguishable ($A_{0\perp}$):

$$A_{0\parallel} = P_1^2 \left\{ g^{(2)}(0) R_2 T_2 \left(R_1^2 \eta_l^2 + T_1^2 \eta_s^2 \right) + R_1 \eta_l T_1 \eta_s \left(T_2 - R_2 \right)^2 \right\} \tag{4.10}$$

$$A_{0\perp} = P_1^2 \left\{ g^{(2)}(0) R_2 T_2 \left(R_1^2 \eta_l^2 + T_1^2 \eta_s^2 \right) + R_1 \eta_l T_1 \eta_s \left(T_2^2 + R_2^2 \right) \right\} \tag{4.11}$$

4.2.3 HOM visibility and indistinguishability

As stated before, an important use of the Mach-Zehnder interferometer is to measure the single-photon indistinguishability of a single-photon source. This is generally done by linking the indistinguishability M to the Hong-Ou-Mandel interference visibility $\mathcal{V}_{\mathrm{HOM}}$ [61, 64, 66]. However, most of these contributions assume that the interferometer is perfectly balanced in intensity and the beam splitters are exactly 50:50. Here we develop a more general expression. The HOM visibility is defined as a function of the correlations at $\Delta\tau = 0$ for distinguishable ($\perp$) and indistinguishable ($\parallel$) photons normalized to the coincidences for the distinguishable case:

$$\mathcal{V}_{\mathrm{HOM}} = \frac{g_{\perp}^{(2)}(0) - g_{\parallel}^{(2)}(0)}{g_{\perp}^{(2)}(0)} \tag{4.12}$$

The necessary correlations can be calculated from our results above as $g_{\perp}^{(2)}(0) = A_{0\perp}/A_{\pm}$ and $g_{\parallel}^{(2)}(0) = A_{0\parallel}/A_{\pm}$.

Equations 4.10 and 4.11 describe the cases of either fully indistinguishable or fully distinguishable photons. To account for experimental imperfections in wavefunction overlap, we extend this model to arbitrary degrees of distinguishability and replace M by MV_p, where the polarization overlap V_p is controlled experimentally. By linear interpolation we obtain a general expression for the correlations at $\Delta\tau = 0$:

$$A_0 = MV_p A_{0\parallel} + (1 - MV_p) A_{0\perp} \tag{4.13}$$

Experimentally, to measure the HOM visibility Eq. 4.12, we determine the two-photon correlations for both maximum and minimum wavefunction overlap. For minimum overlap, the polarization state in one arm of the interferometer is set orthogonal to that in the other; for maximum overlap, the polarization states in both interferometer arms are identical. To account for imperfections in the polarization alignment, we distinguish between the two cases by defining separate polarization overlaps: $V_{p,\parallel}$ for the parallel configuration, and $V_{p,\perp}$ for the orthogonal one. These are substituted into Equation 4.13 in place of V_p when calculating A_0 for $g_{\parallel}^{(2)}(0)$ and $g_{\perp}^{(2)}(0)$. Usually, the values of $V_{p\parallel}$ and $V_{p\perp}$ are close to 1 and 0, respectively. With this we finally derive a general expression for the indistinguishability M as a function of the HOM visibility and all parameters of the MZI (a step by step derivation of this final expression is given in Appendix 4.6.1):

$$M_{\text{full}} = \frac{\mathcal{V}_{\text{HOM}}\left[T_1\eta_s R_1\eta_l\left(T_2^2+R_2^2\right)+g^{(2)}(0)R_2T_2\left(T_1^2\eta_s^2+R_1^2\eta_l^2\right)\right]}{2T_1\eta_s R_1\eta_l R_2T_2\left[V_{p\parallel}-V_{p\perp}\left(1-\mathcal{V}_{\text{HOM}}\right)\right]} \tag{4.14}$$

Comparison to literature

If we use the assumptions of an ideal interferometer, with balanced transmission ($\eta_s = \eta_l$), perfect beam splitters ($R_1 = T_1 = R_2 = T_2 = 1/2$) and perfect polarization state overlap ($V_{p\parallel} = 1$ and $V_{p\perp} = 0$), Eq. 4.14 reduces to

$$M_{\text{simple}} = \mathcal{V}_{\text{HOM}}\left(1+g^{(2)}(0)\right). \tag{4.15}$$

This is in perfect agreement with results presented in Refs. [61–64,73]. However, our result differs by a factor 2 with the expressions for the indistinguishability used in Refs. [66,74], caused by a difference in the multi-photon part of the derivation (last term of Eq. 4.4). We have analyzed the case and found that the resulting error is small for single-photon sources with high single-photon purity, as is the case case in Refs. [66, 74] - but it still leads to an overestimation of the photon indistinguishability of 1.9%.

4.3 Experiment

We now discuss our experimental setup and procedure.

4.3.1 Experimental setup

Excitation scheme

The quantum dot is excited resonantly using a narrow-linewidth frequency-tunable continuous-wave (CW) laser out of which short pulses are carved using two cascaded electro-optic modulators (EOMs) controlled by custom-made electronics [72] (Fig. 4.5). This enables tunability of both the pulse period and pulse widths at a well-defined center wavelength.

The quantum dot device

The quantum dot itself is a negatively charged self-assembled InGaAs/GaAs dot embedded in a microcavity [66, 75–77]. A 31.8 nm thick tunnel barrier separates the p-i-n junction from the electron reservoir enabling quantum-confined Stark effect tuning of the QD resonance wavelength at around 935 nm [71, 77, 78]. The quantum dot is kept at a temperature around 4 K in a closed-cycle cryostat with optical access. The resonant excitation laser light is focused on the quantum dot by an aspheric lens (Thorlabs A240-B) which is placed inside the cryostat to minimize loss of single-photons. The excitation laser is filtered out using a polarization extinction method (PE and PD in Fig. 4.5) enabling extinction of the order of 10^{-6} [79], and the single-photons are collected in a polarization maintaining (PM) single mode fiber.

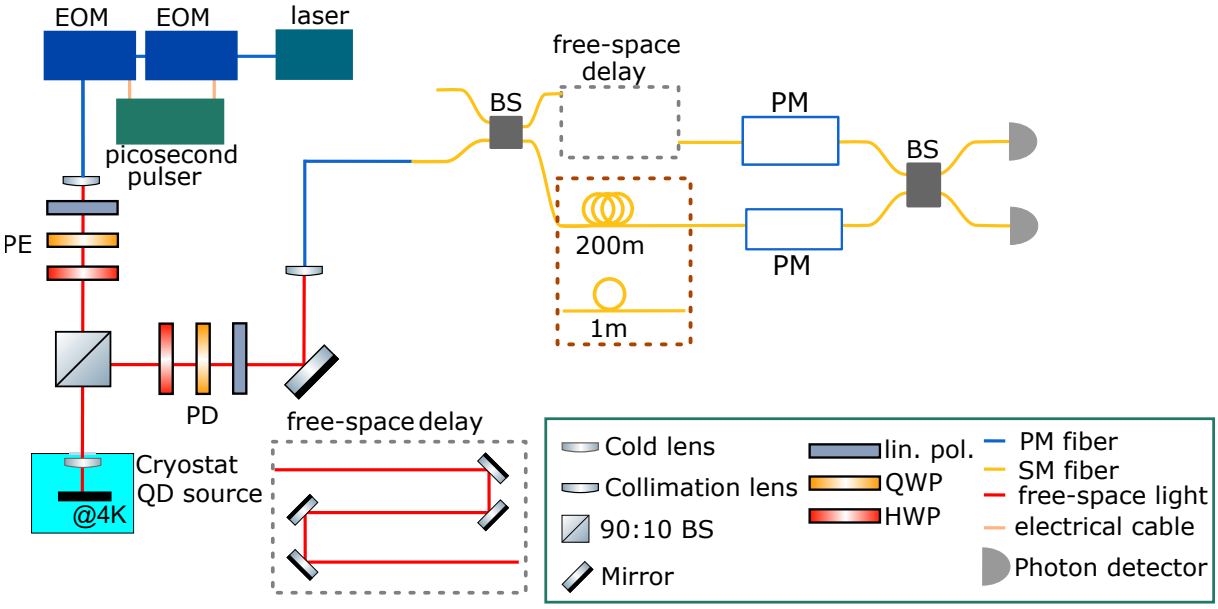

Figure 4.5: Schematic of the experimental setup. Two cascaded electro-optic modulators (EOMs) are used to generate picosecond pulses for excitation of the quantum dot. The polarization state of the excitation laser is optimized in the excitation path (PE) and the excitation laser is filtered out through cross polarization in the detection path (PD). The Mach-Zehnder interferometer consists of two beam splitters (BS) and either has an optical path length difference of 9 ns ($\sim$ 1.8 meters) or 1 µs (200 m). A polarization modulator (PM) in each arm is used to modulate the polarization state overlap V_p

The Mach-Zehnder interferometer

The interferometer shown in Fig. 4.5 consists of two approximate 50:50 fiber-based beam splitters (BS, Thorlabs A240-B for the short delay and OZ Optics FUSED-22 for the long delay). In the lower arm of the interferometer, additional optical fiber of 1 m or 200 m introduces a path delay, which is fine-tuned by the tunable free-space delay in the upper arm. A fiber-based polarization modulator (PM; Polarite III PCD-M02) is placed in both arms of the interferometer to tune the polarization state overlap at the second fiber splitter such that both $g_{\parallel}^{(2)}$ and $g_{\perp}^{(2)}$ can be measured. The photons are detected by two avalanche single-photon detectors (Excelitas SPCM-AQRH-14-FC-ND) and we use a time-tagging card (Cronologic HPTDC, 100 ps resolution) together with custom software to record 2-fold coincidence detection events.

4.3.2 Experimental procedure

The temporal overlap between photons traveling through the two arms of the MZI is optimized by tuning the free-space delay in the upper arm of the interferometer. First we use short laser pulses in combination with low-jitter (40 ps) single-photon detectors and a different correlation card (Becker Hickl SPC-130) for a coarse alignment, and then we fine-tune the temporal alignment by optimizing HOM interference of photons from our single-photon source. For measuring the single-photon purity of the single-photon source with a HBT measurement, we block the free-space delay. For the HOM measurement we tune the polarization state overlap with the polarization modulators; the polarization condition is characterized before and after the experiment, with the use of a polarimeter (Thorlabs PAX1000IR1), to asses polarization drifts.

4.4 Results

The measured two-photon correlations for both the short (9 ns) and long (1 μs) delay in the Mach-Zehnder interferometer are shown in Fig. 4.6, where in panels (a) and (c) the polarization in both arms of the interferometer is set to be the same ($\parallel$), and in (b) and (d) orthogonal ($\perp$). For the short (long) delay experiments we used a laser excitation pulse period of 9 ns (4 ns), a laser pulse width of 58 ps (47 ps), and an integration time of 3 minutes (5 minutes).

In Fig. 4.6 we use the same color scheme as before in Figures 4.1 and 4.3, where red denotes the correlations at $\Delta\tau = 0$, purple the correlations at $\Delta\tau = \pm t_d$ (where $t_d \approx 8.95$ ns for the short delay and $t_d \approx 995.35$ ns for the long delay), and blue corresponds to all other correlations. The values of all relevant correlations are shown in Table 4.1, for which we used a time-bin width of 2 ns. A nonzero background can be observed for all four of the correlation measurements, this is caused by leakage of the excitation laser light due to imperfect cross-polarization filtering and reduced contrast of the excitation laser pulses.

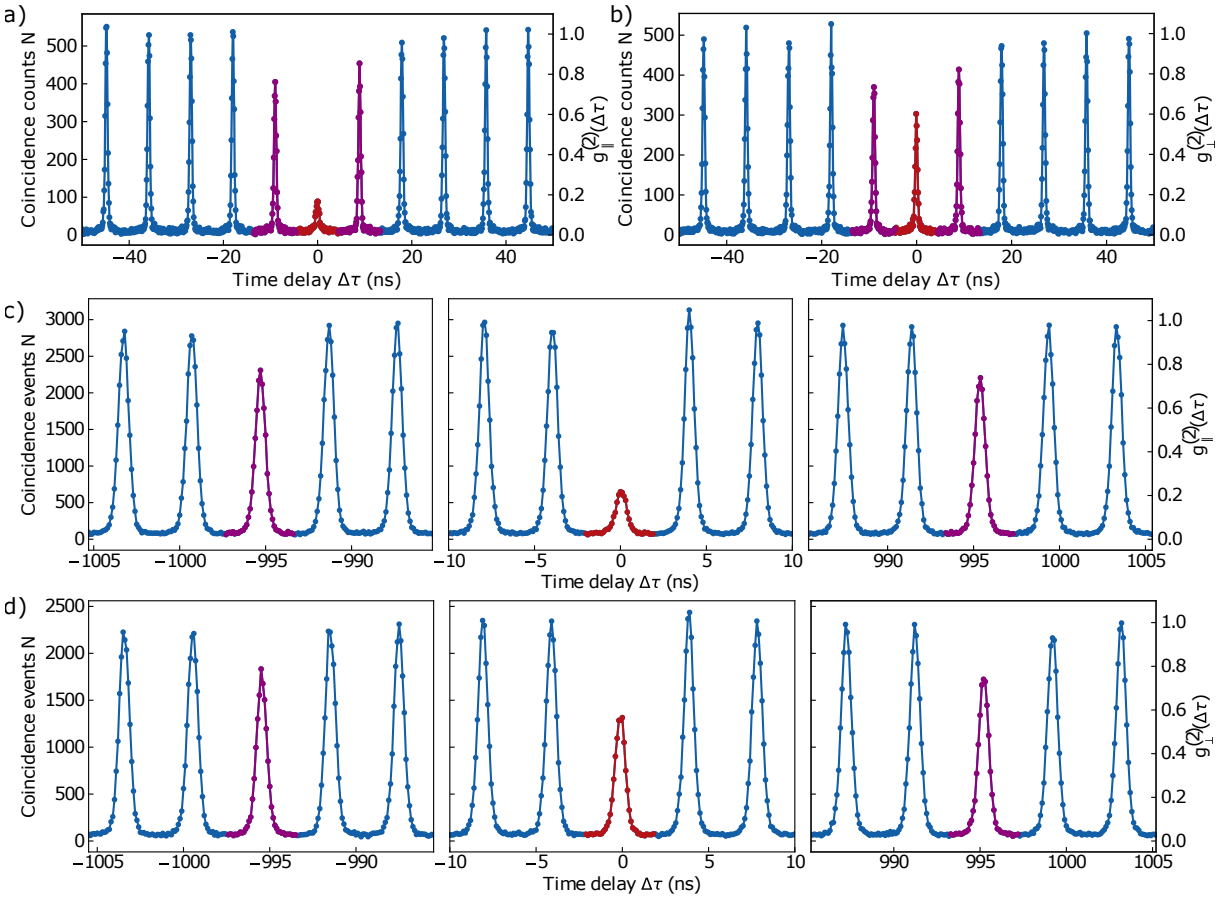

Figure 4.6: Two-photon correlations for both maximized ($\parallel$) and minimized ($\perp$) wavefunction overlap for 9 ns (a & b) and 1 µs (c & d) delay in the MZI.

	short delay (9 ns)			long delay (1 µs)		
	measured		model	measured		model
	$g^{(2)}_{\parallel}$	$g^{(2)}_{\perp}$		$g^{(2)}_{\parallel}$	$g^{(2)}_{\perp}$	
$g^{(2)}_{\parallel}(0)$	0.255±0.009	-	0.245	0.237±0.004	-	0.239
$g^{(2)}_{\perp}(0)$	-	0.608±0.017	0.586	-	0.609±0.007	0.616
$g^{(2)}(+t_d)$	0.824±0.020	0.841±0.022	0.828	0.788±0.008	0.783±0.009	0.803
$g^{(2)}(-t_d)$	0.760±0.019	0.777±0.020	0.763	0.804±0.008	0.799±0.009	0.815

Table 4.1: Comparison between the measured $g^{(2)}$ values for $\Delta\tau = 0$ and $\Delta\tau = \pm t_d$ and the outcome of the model using M_{full}.

From the two-photon correlations we calculate the single-photon indistinguishability M using the method explained in Section 4.2, the results are shown in Table 4.2. We compare the measured HOM interference visibility with the simplified expression assuming an ideal interferometer (Eq. 4.15) and the full expression (Eq. 4.14). From the comparison between $\mathcal{V}_{\text{HOM}}$ with M_{simple} we see that in our case, the purity has a significant impact

	9 ns	1 µs
$\mathcal{V}_{\mathrm{HOM}}$	0.581	0.612
M_{simple}	0.690	0.757
M_{full}	0.834	0.770

Table 4.2: Comparison of the Hong-Ou-Mandel visibility $\mathcal{V}_{\mathrm{HOM}}$ and the extracted indistinguishability comparing the standard simple calculation which is assuming a perfect MZI M_{simple} (Eq. 4.15) with the outcome of the full calculation without assumptions on the experimental parameters M_{full} (Eq. 4.14). All experimental parameters are given in Appendix 4.6.2.

on the estimation of the indistinguishability of the single-photon source. Furthermore, we see that the difference between outcomes of M_{simple} and M_{full} for the longer delay is quite small (0.013), while for the shorter delay the difference is much more significant (0.144). The biggest difference between the two sets of measurements is that for the longer delay the polarization state stability for the duration of the measurement was better with a shift in polarization of 1.4%, while the short-delay experiment had a shift in polarization of 30.3%. Because only the full model takes this polarization shift into account only the M_{full} for 9 ns photon separation is higher than for 1 µs as expected.

Next to the calculation of the indistinguishability, we compare the measured and modeled values of the second-order correlation function measured at $\Delta\tau = 0$ and $\Delta\tau = \pm t_d$ in Table 4.1. As stated before, the modeled $g^{(2)}$ values are calculated by using the appropriate expression for A (Eqs. 4.5, 4.6, 4.10, 4.11) and divide it by the expression for the side-peaks used for normalization $A_{\pm}$ (Eq. 4.3). We see that the model is in very good agreement with the measured data where all model outcomes fall within or are close to the error margin of the measured values. The errors are not taking into account inaccuracies of the measured values of the MZI parameters such as transmission.

Comparing the value of $g^{(2)}(\pm t_d)$ for both interferometers, we find that there is a greater asymmetry for the short delay MZI ($|g^{(2)}(t_d) - g^{(2)}(-t_d)| \approx 0.064$) than for the long delay MZI ($|g^{(2)}(t_d) - g^{(2)}(-t_d)| \approx 0.016$), which is also clearly visible in Fig. 4.6. Interestingly, this height difference is exactly the same for the $\parallel$ and $\perp$ measurements. The most significant contribution is the imbalance in the second beam splitter which is greater in the short delay measurement ($R_2 = 0.54$) than in the long delay measurement ($R_2 = 0.492$). The difference between the reflection and transmission coefficients between the two interferometers is not large ($< 5\%$) but it shows that the $g^{(2)}(\pm t_d)$ correlations are quite sensitive to this imbalance, more than the $g^{(2)}_{\parallel,\perp}(0)$ correlations are.

4.5 Conclusions and outlook

We have examined a single-photon stream in a Mach-Zehnder interferometer (MZI) beyond assessing photon indistinguishability by Hong-Ou-Mandel two-photon correlations. We highlighted that the correlations observed in such setup carry more information than just the overlap of single-photon wave packets, and that experimental imperfections should be taken into account. First, for a perfect interferometer, we explained intuitively the

correlations for a time difference equal to the delay between the interferometer arms $\Delta\tau = \pm t_d$. Then, we developed an analytic model that takes many experimentally relevant parameters into account, explaining the three different classes of correlations: the center correlations at $\Delta\tau = 0$, the correlations corresponding to the interferometer time-delay at $\Delta\tau = \pm t_d$, and all other correlations. We obtained a generalized description of the indistinguishability M as a function of properties that are important for any Mach-Zehnder interferometer experiment. Simplifying the expression for M for an ideal experiment results in the known expression [61–64, 68, 73]. We apply our theory to experimental data obtained with a quantum dot - microcavity single-photon source and a Mach-Zehnder interferometer with both short (9 ns) and a long (1 µs) delays. We observe very good agreement for all correlations. Our clear formulas and model taking experimental imperfections into account might be broadly useful for photonic quantum information research and applications. A similar model could be extended to multi-photon interference in a Sagnac interferometer [71]. This knowledge is essential for error-benchmarking in probabilistic-gate linear cluster state generation schemes [80, 81].

4.6 Appendix

4.6.1 HOM visibility and indistinguishability

Here we show details on the derivation of the final expression for the indistinguishability M_{full} (Eq. 4.14 in the main text). Equation 4.13 in the main text shows that for an arbitrary polarization state overlap the correlation probability at $\Delta\tau = 0$ can be written as:

$$A_0 = MV_pA_{0\parallel} + (1 - MV_p)\, A_{0\perp} \tag{4.16}$$

where V_p is the polarization state overlap of the photons in the different arms of the interferometer and $A_{0\parallel}$ and $A_{0\perp}$ are the correlations at $\Delta\tau = 0$ for fully indistinguishable ($\parallel$) or fully distinguishable ($\perp$) photons:

$$\begin{aligned} A_{0\parallel} =& P_1^2 \left\{ g^{(2)}(0) R_2 T_2 \left(R_1^2\eta_l^2 + T_1^2\eta_s^2 \right) + R_1\eta_l T_1\eta_s \left(T_2 - R_2 \right)^2 \right\} \\ A_{0\perp} =& P_1^2 \left\{ g^{(2)}(0) R_2 T_2 \left(R_1^2\eta_l^2 + T_1^2\eta_s^2 \right) + R_1\eta_l T_1\eta_s \left(T_2^2 + R_2^2 \right) \right\} \end{aligned} \tag{4.17}$$

If we substitute the expressions from Eq. 4.17 into Eq. 4.16 we obtain after simplification

$$A_0 = P_1^2 \left\{ g^{(2)}(0) R_2 T_2 \left(R_1^2\eta_l^2 + T_1^2\eta_s^2 \right) + R_1\eta_l T_1\eta_s \left(T_2^2 + R_2^2 \right) - 2MV_pR_1\eta_l T_1\eta_s R_2 T_2 \right\}. \tag{4.18}$$

The definition of the HOM interferometric visibility is

$$\mathcal{V}_{\text{HOM}} = \frac{g_\perp^{(2)}(0) - g_\parallel^{(2)}(0)}{g_\perp^{(2)}(0)}, \tag{4.19}$$

where the necessary correlations can be calculated from our analysis as $g_\perp^{(2)}(0) = A_0(V_{p\perp})/A_\pm$ and $g_\parallel^{(2)}(0) = A_0(V_{p\parallel})/A_\pm$. Therein, for example, $A_0(V_{p\perp})$ is the expression given in 4.18 for the measured polarization state overlap when polarization states in the two arms of the interferometer were set to be orthogonal. Inserting these definitions into the definition of $\mathcal{V}_{\text{HOM}}$ results in

$$\mathcal{V}_{\text{HOM}} = \frac{2MR_1\eta_l T_1\eta_s R_2 T_2 \left(V_{p\parallel} - V_{p\perp} \right)}{g^{(2)}(0) R_2 T_2 \left(R_1^2\eta_l^2 + T_1^2\eta_s^2 \right) + R_1\eta_l T_1\eta_s \left(T_2^2 + R_2^2 \right) - 2MV_{p\perp}R_1\eta_l T_1\eta_s R_2 T_2}. \tag{4.20}$$

The final step is to rewrite Equation 4.20 to obtain the expression for indistinguishability

$$M_{\text{full}} = \frac{\mathcal{V}_{\text{HOM}} \left[T_1\eta_s R_1\eta_l \left(T_2^2 + R_2^2 \right) + g^{(2)}(0) R_2 T_2 \left(T_1^2\eta_s^2 + R_1^2\eta_l^2 \right) \right]}{2T_1\eta_s R_1\eta_l R_2 T_2 \left[V_{p\parallel} - V_{p\perp} \left(1 - \mathcal{V}_{\text{HOM}} \right) \right]}. \tag{4.21}$$

4.6.2 Experimental parameters

Table 4.3 shows all required experimental parameters to calculate the indistinguishability of our single-photon source using the full model M_{full}, as well as the model outcomes for the two photon correlations at $\Delta\tau = 0$ and $\Delta\tau = \pm t_d$ which are shown in Table 4.1 in the main text.

	short delay (9 ns)	long delay (1 µs)
$g^{(2)}(0)$	0.187±0.015	0.237±0.007
$V_{p\parallel}$	0.846	0.98552
$V_{p\perp}$	0.231	0.00584
R_1	0.47	0.484
T_1	0.53	0.516
η_l	0.627	0.657
η_s	0.602	0.628
R_2	0.54	0.492
T_2	0.46	0.508

Table 4.3: Overview of experimental parameters needed to calculate M_{full} for both the short delay and long delay MZI.